Clay-Polymer Nanocomposites: Morphology, Structure, Properties and Applications

10: Neutron Scattering on different states of polymer/clay compounds: From solution to dry states.

Henrich Frielinghaus[1], Wim Pyckhout-Hintzen[2]

[1]Forschungszentrum Jülich GmbH, Garching, Germany
[2]Forschungszentrum Jülich GmbH, Jülich, Germany

10.1 Introduction

Nanocomposites [1] in general have gained importance in nowadays products leading to improved performance of these complex compound materials. The structure of the solid particles is not limited in terms of shape in advance, but their specific function is tightly connected to their shape. Scattering experiments [2, 3, 4] are often employed to supervise production routes and the final performance, but not all possibilities of scattering experiments are exploited due to several reasons: Engineers need to enter the unknown stage of scattering experiments, and the scattering experts need to simplify their experience to simple usable recipes that are applicable and reliable. This process is still ongoing and the authors hope to contribute to this highly interesting journey.

The advantages [5, 6] of clay-polymer nanocomposites [7] are already explored: mechanical improvements [8, 9], fire retardancy [5], and gas permittivity [10]. A good dispersion state is not always given a priori, and special strategies need to be employed [11, 12]: One might need strong shear fields, or even chemical modifications which either cover the clay with surfactants to reduce the surface tension or directly graft polymers to the particles. The obtained results of such measures need to be explored. Here scattering experiments come into play. They allow for characterizing the dispersion state and give feedback to the dispersion strategy. When employing microscopic models to connect the nanostructure with the macroscopic behavior, new insights might be gained that would allow for predictive tailoring of the macroscopic behavior. For instance the prediction of rheological properties of clay containing systems is still a demanding task.

10.2 Scattering Techniques

Scattering techniques have historically been employed to atomistic structures that have not been accessible by direct imaging techniques at that time [13]. They make use of the wave property of the probe, which then is often regarded as radiation. The interaction of quantum mechanical wave-like particles with matter gives rise to scattering. The careful interpretation of the scattering patterns then allows for concluding on the original structure [14, 15]. This rather indirect view of the real structure makes the technique rather complicated, but it also has its strengths:

1. Most often, the radiation dose rates are such low, that the scattering technique is non-destructive.

2. Most often, reasonable thicknesses for the sample can be chosen. The radiation can penetrate the respective thickness of sample, which otherwise might be inaccessible to other techniques. Also environments for external stimuli are possible, such that in-situ and in-operando experiments can be conducted.
3. Most often, the probed volumes are rather large, such that the obtained structure is highly representative for the distribution of configurations inside the sample.
4. The investigated length scales are given by the wavelength of the probe. While many other direct imaging techniques start to catch up on the nano- and Ångström-scale, scattering is still often the method of choice at small length scales.

A few drawbacks of the scattering method shall not be kept secret:

1. The method is indirect, and some expertise is needed to interpret scattering data well.
2. Since intensities are detected at the end, phases of the scattered radiation field are lost. This results in a certain loss of information, that is often overcome in several ways: (a) complementary techniques are used to such a degree that the results are extremely firm [16], (b) reverse Monte Carlo and maximum entropy techniques display the most probable structures [17, 18, 19, 20], and (c) multi-dimensional contrast variation experiments overcome the phase problem to considerable extent [21].

We will deal with the two problems in the following manner: The main goal of this article is to disseminate the expertise about scattering experiments on systems containing clay particles, such that the reader will be able to obtain important information of his own experiment afterwards. For complementary information, it is often enough to know that the clay particles are platelets. Employing scattering experiments for characterizing clay nanocomposites is not new. Some examples can be found in References [22, 23, 24, 25].

10.3 Small Angle Scattering and Wide Angle Scattering

The two scattering methods at smaller and larger angles have many aspects in common, and only a few additional simplifications apply to the small angles [14]. Both of them imply that the energy after the scattering process is not analyzed, which most often results in a simpler interpretation. Mostly, the investigated structures move on such long time scales that the inelastic scattering process can be neglected for the interpretation, and the experiment aims at the pure structure.

A classical layout of a scattering experiment is displayed in Figure 1. The incident beam is obtained from a radiation source that then is prepared in terms of energy and direction. The monochromator selects a certain energy of the radiation, and the collimation limits the possible directions of the radiation by having at least two apertures at a certain distance *C*. The prepared beam hits the sample, and is either scattered or transmitted by/trough the sample. The transmitted radiation is often not considered in very detail, and therefore is blocked by a beam stop in the straight direction. The detector detects the scattered radiation in terms of intensity as a function of the scattering angle 2θ. Large area detectors cover large solid angles at the same time,

while small detectors need to be moved along a range of scattering vectors. Most often, the collimation distance C is rendered symmetrical to the detector distance D, and the entrance aperture dimension d_E is double the sample aperture size d_S, and comparable to the spatial detector resolution d_D. The described spatial dimensions serve for an optimal intensity at best possible resolution [14, 15] (see also chapter 10.9).

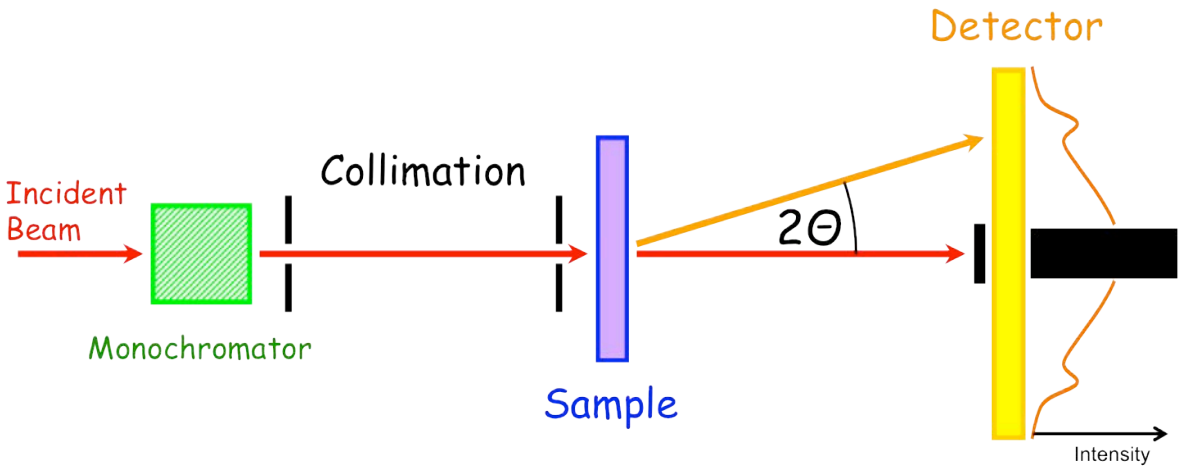

Figure 1: A schematic view on a (small) angle scattering experiment with monochromator, collimation, sample and detector. A typical small angle scattering intensity distribution is depicted right to the detector.

Small angle scattering instruments keep large area detectors around the central beam stop, and therefore collect much scattered intensity simultaneously. Wide angle machines tend to have movable detectors that might be limited to single or several tube detectors.

In order to connect the collected intensity distribution to physical parameters of the sample (namely its structure), the abstract scattering vector Q replaces the scattering angle 2θ in terms of:

$$Q = \frac{4\pi}{\lambda}\sin\theta \tag{1}$$

It carries the reciprocal unit of the radiation wavelength λ, and therefore the Q-space is also called reciprocal space. For small angles, the sin-function is linear, and we can approximate:

$$Q \approx \frac{2\pi}{\lambda}\cdot 2\theta \tag{2}$$

The meaning of the reciprocal space becomes most clear, when the scattering pattern shows peaks. Then, the peak position Q_{max} indicates a preferred length scale ℓ:

$$\ell = 2\pi Q_{max}^{-1}$$

(3)

This concept also holds for characteristic transitions or features in the intensity profiles, which are located at a certain Q-vector. Very often, the numeric prefactor of 2π changes then a little.

Throughout this manuscript we assume the scattering pattern to be isotropic; that means the azimuthal angle of the intensity distribution does not play a role. This often appears even from scattering of platelet particles when the different configurations of several particles appear over all directions. This explains why originally the scattering vector $\vec{Q} \equiv \boldsymbol{Q}$ is a real vector, but practically often reduces to a scalar magnitude Q.

10.3.1 Absolute calibration

While the Q-axis reveals important information about several typical sizes in your sample, the absolute intensity is connected to the absolute scattering power of the structures inside the sample that reveals additional information [14, 15]. In detail, the experimental scattering intensity $I(Q)$ is connected to the macroscopic differential scattering cross section $d\Sigma/d\Omega(Q)$ as follows:

$$I(Q) = I_0 \cdot A \cdot \varepsilon \cdot d \cdot T_r \cdot \Delta\Omega \left(\frac{d\Sigma}{d\Omega}(Q) + B_{\mathrm{bckgr}} \right) \tag{4}$$

For an experiment, one needs to determine the incident intensity at the sample I_0, the irradiated area of the sample A, the detector efficiency ε, the sample thickness d, the transmission of the sample T_r, and the solid angle $\Delta\Omega$, to which the experimental intensity refers. Often, there is a parasitic background intensity B_{bckgr}, which usually is subtracted from the signal for further analysis. The incident intensity is usually indirectly determined through a secondary standard, the scattering of which is measured under the same conditions as the sample such that some dependencies cancel out ($I_0 A \varepsilon$). The resulting macroscopic cross section $d\Sigma/d\Omega(Q)$ is then an instrument-independent information, that for instance tells about the concentration of a solute in solution. Further details are discussed in section 10.4.

10.3.2 The Born approximation

The approximation of Born leads to a theoretical connection between the sample structure and the macroscopic cross section. While there are several simplifications behind, the most important prerequisite for using the Born approximation is the condition that the scattering is weak [13, 14, 15]. This means, that only up to ca. 10% of the scattered intensity may contribute to the macroscopic cross section $d\Sigma/d\Omega(Q)$, often excluding the background intensity. Then, the macroscopic cross section reads:

$$\frac{d\Sigma}{d\Omega}(Q) = \frac{1}{V} \left| \sum_j b_j \cdot \exp\left(i\boldsymbol{Q} \cdot \boldsymbol{r}_j \right) \right|^2 \tag{5}$$

At this point, $d\Sigma/d\Omega(Q)$ is connected to all single atoms of index j with their specific scattering length b_j, and individual complex phases arising from their position $\boldsymbol{r}_j$ (here

we refer to vectors $\boldsymbol{Q}$ and $\boldsymbol{r}_j$ again). This atomistic view is important for structures on the 2-3Å length scale, i.e. $Q \geq 2\text{Å}^{-1}$ [26] (see Figure 2). There are still wide or medium angle scattering experiments aiming at the 10-20Å length scale, i.e. $Q \geq 0.3\text{Å}^{-1}$, where another view on the structures applies: When leaving the atomistic scale towards larger length scales, the individual atom is not important anymore, and the chemical formulae of whole molecules or larger subunits are more essential. This is also the range of small angle scattering experiments ($Q \leq 0.3\text{Å}^{-1}$). The macroscopic cross section reads then:

$$\frac{d\Sigma}{d\Omega}(Q) = \frac{1}{V}\left|\int_V d^3r \;\; \varrho(\boldsymbol{r}) \cdot \exp(i\boldsymbol{Q}\boldsymbol{r})\right|^2 \tag{6}$$

Essentially, the individual scattering length b_j is replaced by a scattering length density $\rho(\boldsymbol{r})$, and the sum is exchanged by an integral. As explained before, now whole molecules or larger subunits describe a field of the scattering length density:

$$\rho_k = \frac{1}{V_k}\sum_j b_{jk} \tag{7}$$

where the sum runs over all atoms of number j in the molecule k. So, here several atoms indexed by j of type k are collectively considered. The specific volume of subunit k is V_k. Practically, for solvents, each molecule is a subunit, and the specific volume is calculated from the density. For polymers, the monomer (or more precisely: the repeat unit) is usually chosen as the subunit. For clay particles, the best scattering length density is based on the overall chemical formula of the silicate, and internal lateral inhomogeneities are neglected. One might observe them in a dedicated contrast matching measurement [27] where then residual scattering occurs. The detailed analysis of such inhomogeneities though is beyond the scope of this manuscript.

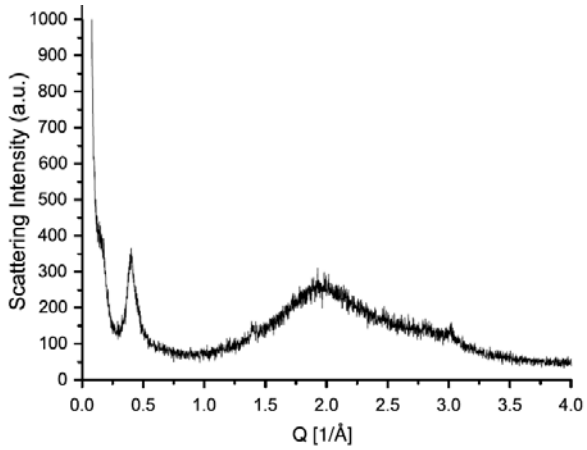

Figure 2: A WAXS experiment on MMT clay dispersed in water. One observes peaks in the classical WAXS range Q = 1.4, 2.0 and 3.0Å^{-1} for atomistic structures, but also at intermediate angles Q = 0.4Å^{-1} for the stacking of several platelets. From Ref. [27].

10.4 The scattering of simple particles

The power of neglecting single atoms is found then, when simple shapes of internal homogeneity are considered. The essential equation for the macroscopic cross section is then found to be [14, 15)]:

$$\frac{d\Sigma}{d\Omega}(Q) = (\Delta\varrho)^2 \cdot \phi \cdot V_{\text{particle}} \cdot F^2(Q) \tag{8}$$

The important prefactors are the contrast arising from the scattering length density difference $\Delta\varrho = \varrho_1 - \varrho_2$ of the colloids and the surrounding matrix (be it solvent or polymer), the concentration of the colloids ϕ, and the volume of a single colloidal particle V_{particle}. The only Q-dependence lies in the form amplitude $F(Q)$, the square of which is called form factor. The low Q limit of the form amplitude is 1, and so a calibrated scattering experiment allows for crosschecking of the sheer particle volume with the shape observed in $F(Q)$. Another crosscheck might aim at the concentration.

While the major part of this manuscript aims at platelets, the simplest colloidal structure is a sphere. For the form amplitude one obtains the simple analytical formula [28]:

$$F(Q) = 3 \cdot \frac{\sin(QR) - (QR)\cos(QR)}{(QR)^3} \tag{9}$$

This dependence is displayed in Figure 3 on a double logarithmic scale. While the red curve indicates the original formula with heavy oscillations (called fringes) at larger scattering vectors, the blue curve indicates a practical measurement with a certain distribution of radii R and/or finite instrumental resolution (see also chapter 10.9). In both cases we have a Guinier range at lowest $Q < 0.02\text{Å}^{-1}$, and a Porod range at higher $Q > 0.07\text{Å}^{-1}$. The distribution of length scales, may it arise from R or Q, smears the fringes over a certain range, and accordingly more or less fringes remain to be seen. The Guinier scattering is often expressed in a simplified way, that holds for small Q, and it reads [14, 15, 29]:

$$\frac{d\Sigma}{d\Omega}(Q) = (\Delta\varrho)^2 \cdot \phi \cdot V_{\text{particle}} \cdot \exp\left(-\frac{R_g^2 Q^2}{3}\right) \tag{10}$$

While the prefactors remain as for the original formula with the volume of a single spherical colloid $V_{\text{particle}} = 4\pi R^3/3$, the form factor is approximated by a simple Gaussian. This expression introduces a new aspect of the colloidal size, namely the radius of gyration R_g. It is connected to the second moment of the mass distribution of the colloid (similar to the moment of inertia). For spherical homogenous colloids the relation $R_g = \sqrt{3/5} \cdot R$ holds. Applying the Guinier expression to any other scattering curve at small Q will still provide a radius of gyration, but the meaning has to be analyzed in context with the colloidal shape and volume.

The first minimum of the scattering curve is often visible for spherical colloids, because the distribution of length scales usually is good enough, and the radius of the colloid can

be determined according to $Q_{\min} = 4.493/R$. This formula is another example reciprocal space relations (see also eq. 3), where the prefactor has changed slightly from the original value 2π. For consistency, the radius determined by the first minimum can be crosschecked with the radius of gyration, and the colloidal volume. If there are strong inconsistencies, the shape might be non-spherical, and other models have to be considered.

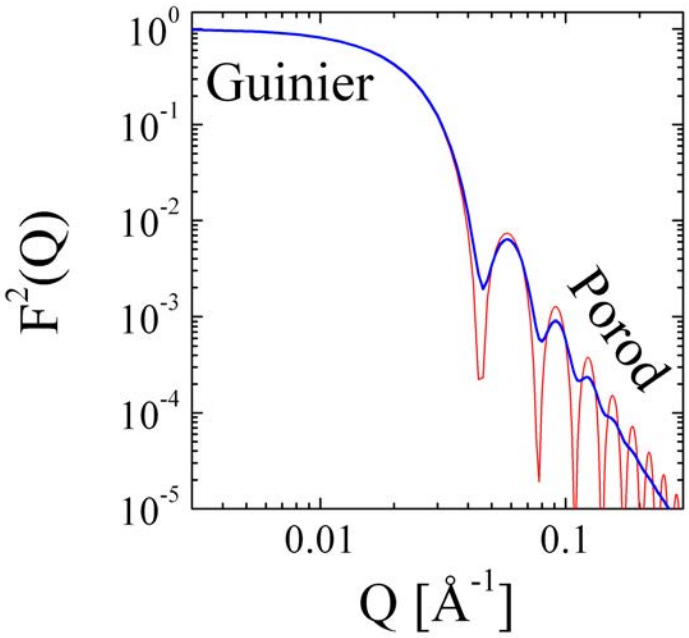

Figure 3: The form factor of a spherical colloid with the radius 100Å (red line). The Gunier range is found at small Q, while the Porod range is at high Q. For polydisperse spheres and/or finite instrumental resolution, the blue line is obtained with the linear asymptote in the double logarithmic scale.

The Porod formula is usually expressed for the Q-range where the fringes have been smeared out to yield a straight line in the double logarithmic plot. It simply reads:

$$\frac{d\Sigma}{d\Omega}(Q) = P \cdot Q^{-4} \tag{11}$$

The Porod constant $P = 2\pi(\Delta\varrho)^2 S_{\text{tot}}/V_{\text{tot}}$ is connected to the characteristic surface S_{tot}, and reads for spherical colloids $P = 6\pi(\Delta\varrho)^2\phi/R$. Again, this gives rise to crosschecks with the radii determined at different Q-ranges. Independent from the spherical model that we discuss here, the connection of the Porod constant with the characteristic surface holds for other structures [14, 29]. The prerequisite of applying this scattering law is the sharp transition of scattering length densities between clearly separated domain structures, i.e. volumes. We will see in the following that other scattering (Porod) laws may occur for different structures.

The next stage of complexity in the scattering occurs for platelets. Often, the structure is approximated by flat cylinders. The general form amplitude for a cylinder with the main axis along the z-axis reads [28]:

$$\hat{F}(Q,\varphi,\vartheta) = \frac{\sin(QH\cos\vartheta)}{QH\cos\vartheta} \cdot 2\frac{J_1(QR\sin\vartheta)}{QR\sin\vartheta} \tag{12}$$

The polar angle between $\boldsymbol{Q}$ and the z-axis is ϑ. The two factors arise from the two different structures in different directions: the finite length of the cylinder d with the height parameter $H = d/2$, and the circular structure with the radius R. There is no dependence on the azimuthal angle φ due to the cylinder symmetry. For platelets, the relation $R \gg H$ holds. For oriented platelets, the scattering would be anisotropic, and the discussion would stop here. But in practice, the platelets do often not have a preferred orientation, and the orientational averaging needs to be applied to the model, according to:

$$F^2(Q) = \frac{1}{2\pi}\int_0^{2\pi} d\varphi \int_0^{\frac{\pi}{2}} d\vartheta \;\; \hat{F}^2(Q,\varphi,\vartheta)\sin\vartheta \tag{13}$$

When the original form amplitude is independent of the azimuthal angle φ, its integral cancels with the prefactor. The averaging over the polar angle remains for platelets, and practically is done numerically when this model is applied to scattering curves. Only when the *separation of length scales* applies ($R \gg H$), a further simplification is found:

$$F^2(Q) = \frac{2}{Q^2R^2} \cdot \left(1 - \frac{J_1(2QR)}{QR}\right) \cdot \frac{\sin^2(QH)}{Q^2H^2} \tag{14}$$

We identify the first two factors with the orientationally averaged circular structure, while the third factor arises from the finite thickness without changes. The concept of unchanged scattering functions for the small length scales is also found for other models, for instance for chain structures with finite cross section [30].

Graphically, the simplified scattering function and the original view with explicit orientational averaging cannot be distinguished as seen in Figure 4 (for R = 600Å and H = 5Å). We identify four different Q-ranges: The Guinier range ($Q < 0.003\text{Å}^{-1}$) for the overall particle is connected to the particle volume $V_{\text{particle}} = 2\pi R^2 H$ and the radius of gyration $R_g = \sqrt{R^2/2 + H^2/3}$ according to the original formula of eq. 10. The first power law region ($0.008\text{Å}^{-1} < Q < 0.2\text{Å}^{-1}$) describes the shape of an infinitely thin platelet with typical thickness:

$$\frac{d\Sigma}{d\Omega}(Q) = 4\pi \cdot (\Delta\varrho)^2 \cdot \phi \cdot \frac{H}{Q^2} \tag{15}$$

This scattering law is connected to the fractal structure of a thin surface in a 3d volume. The next region is the Guinier region ($0.2\text{Å}^{-1} < Q < 0.5\text{Å}^{-1}$) that observes the finite thickness of the platelet. This scattering law is considerably different from the original Guinier expression (eq. 10), because the surface and the finite thickness appear at the same time.

$$\frac{d\Sigma}{d\Omega}(Q) = 4\pi \cdot (\Delta\varrho)^2 \cdot \phi \cdot \frac{H}{Q^2} \cdot \exp\left(-\frac{1}{3}Q^2H^2\right) \tag{16}$$

At highest $Q > 1\text{Å}^{-1}$ the volume property of the platelet appears. So the considered length scales are such small, that a small portion of the interface between the colloid and the matrix is not correlated anymore to other interface portions. One simply finds the Porod constant:

$$P = 2\pi(\Delta\varrho)^2\phi \cdot \left(\frac{1}{H} + \frac{2}{R}\right) \approx 2\pi(\Delta\varrho)^2\phi/H \tag{17}$$

At some point in this Q-range, the atomistic structures would also superimpose, and the idealized platelet structure would not be observed as pure as discussed here.

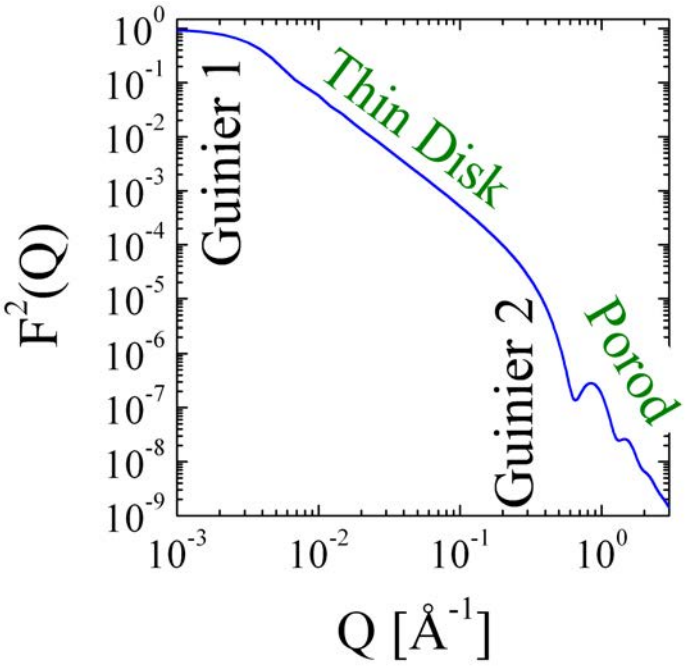

Figure 4: The form factor of a platelet with radius R = 600Å and a thickness of $2H$ = 10Å. One can identify several Q-ranges that express the fractal structure of a platelet as described in the text.

10.5 More complicated, but less specific structures

We have seen in the previous chapter that often a *separation of length scales* occurs. The scattering of such structures then results in well-separated Q-ranges, where simple power-laws such as Q^{-D_f} appear. The exponent D_f is the fractal dimension of the structure, and can take values limited between 1 and 6 (typically $D_f \leq 4.5$). For the direct observation of mass fractals, D_f is the dimensionality of the fractal structure (1 for rods, 2 for surfaces, 3 for a house of cards), while $D_f = 2d - D$ holds for surface fractals with the dimensionality D in d dimensions. So the classical Porod exponent of 4 relates to a 3-dimensional structure (d = 3), the surface (D = 2) of which is observed. Further

roughness would even result in higher exponents, but if the surface is completely diffuse, the power law disappears, and a bare Gaussian decay with a roughness parameter σ remains only.

More precisely, we have seen that the *separation of length scales* results in an alternating sequence of Guinier and power law scattering. For many structures with a wider distribution of length scales (polydispersity), there are no more fringes in between the Guinier range and the power law, and the curves look quite smooth on a double logarithmic plot. Here comes the idea of Beaucage into play [31]. For a single size with a single fractal structure, the following – rather heuristic – scattering formula is obtained:

$$\frac{d\Sigma}{d\Omega}(Q) = G_1 \exp\left(-\frac{1}{3}Q^2R_g^2\right) + B_1\left(\frac{\mathrm{erf}^3(QR_g/\sqrt{6})}{R_gQ}\right)^{D_f} \tag{18}$$

The prefactor G_1, as we have learned, is connected to several magnitudes (namely contrast, concentration and particle volume, see eq. 8), and the radius of gyration R_g can be connected to the particle size, if its geometry is known. The prefactor B_1 might be connected to G_1, if a Benoît mass fractal is described, according to $B_1 = G_1\Gamma(D_f/2)D_f$; otherwise B_1 stays slightly below that value. Empirically, the argument of the error function erf(x) usually is multiplied by a factor of 1.06. The formula was then expanded to several stages of fractal structures. For those hierarchical structures one finds:

$$\frac{d\Sigma}{d\Omega}(Q) = \left[\left[G_1 \exp\left(-\frac{1}{3}Q^2R_1^2\right) + B_1\left(\frac{\mathrm{erf}^3(QR_1/\sqrt{6})}{R_1Q}\right)^{D_1} + G_2\right]\exp\left(-\frac{1}{3}Q^2R_2^2\right) + B_2\left(\frac{\mathrm{erf}^3(QR_2/\sqrt{6})}{R_2Q}\right)^{D_2} + G_3\right]\cdots \tag{19}$$

The two square brackets and the indices *i* indicate the different stages of fractal structures, ranging with *i* from large to smaller structures. By employing more brackets and more indices *i*, the formula can be naturally expanded to an arbitrary number of fractal stages. Compared to our model platelet, the Beaucage fractal description allows for more parameters to be adjusted. So, by applying this model, one might be left with uncertainties in the interpretation which exact structure is connected to which length scale. This Beaucage model fitting basically corresponds to a ruler based analysis in a log-log-plot of the scattering curve, where the intersections are connected to the typical length scales (here called R_i).

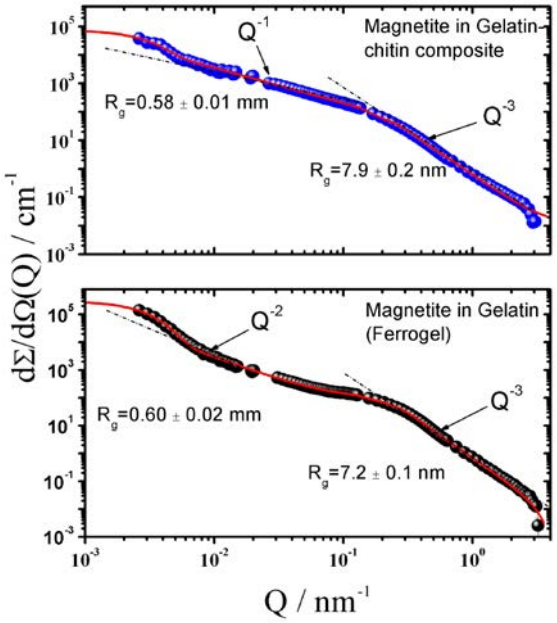

Figure 5: Scattering of magnetite particles in different environments: (top) a gelatin/chitin composite, and (bottom) a pure gelatin gel. The largest length scales (R_g) are µm and not mm as indicated at lowest Q. Taken from Ref. [32].

Now, we discuss a system with chitin platelets that are embedded in a gelatin/water gel [32]. The system mimics natural nacre that can also be obtained by using clay instead of chitin [33]. The platelet concentration is such high, that locally all platelets are aligned in parallel. Rendering a certain heavy water content, the main focus of the experiment was on the magnetite particles that are captured in between the platelets (Figure 5). For comparison the same particles were studied in the gelatin gel without chitin. The isolated magnetite particles are observed a high $Q > 0.2\text{nm}^{-1}$ with a power law of Q^{-3} that takes account for the interstitial between the touching particles. At intermediate Q ($0.01\text{nm}^{-1} > Q > 0.2\text{nm}^{-1}$) the fractal structure of the magnetite chains becomes visible. Within the chitin platelets, the chains are stretched and rod-like (with an exponent 1), while in the pure gelatin gel, the chains are polymer- or coil-like (with an exponent 2, as we will see in chapter 10.7). At very low $Q < 0.005\text{nm}^{-1}$, the branching of the different chains leads to network with a finite correlation length ξ, that gives rise to a Guinier scattering ~exp $(-\xi^2 Q^2)$ with $\xi = R_g/\sqrt{3}$.

10.6 The Role of the Structure Factor

When we discussed the scattering of simple particles, we assumed that they appeared uncorrelated in the sample volume. Only then, the scattering intensity of individual particles superimposes independently (as seen by the factor ϕ in eq. 8). For concentrated or attractive particles, the correlation between the different particles has to be taken into account, because certain distances appear to be more preferred. This gives rise to an additional factor, the structure factor $S(Q)$, and the original formula 8 transfers to [14, 15, 29]:

$$\frac{d\Sigma}{d\Omega}(Q) = (\Delta\varrho)^2 \cdot \phi \cdot V_{\text{particle}} \cdot S(Q) \cdot F^2(Q) \tag{20}$$

The theory of the structure factor might be seen as complicated. So we will come to some simple expressions after we have summarized the essential ingredients. The simplest theoretical approach to the structure factor is obtained by discussing the pair correlation function $g(\boldsymbol{r})$. Except for some peculiarities about Fourier transformations of constants, the structure factor $S(Q)$ is basically the Fourier transformation of $g(\boldsymbol{r})$:

$$S(Q) = 1 + \phi \int_V d^3r \; (g(\boldsymbol{r}) - 1) \; \exp\left(i\boldsymbol{Q}\boldsymbol{r}\right) \tag{21}$$

We see the subtraction and addition of 1 at two places, which takes care of unwanted divergences (and the self-correlation). Otherwise a simple Fourier transformation remains. The pair correlation function is simply defined by probabilities, and reads:

$$g(\boldsymbol{r}_2 - \boldsymbol{r}_1) = \frac{P(\boldsymbol{r}_1, \boldsymbol{r}_2)}{P(\boldsymbol{r}_1) \cdot P(\boldsymbol{r}_2)} \tag{22}$$

with the probability of finding any single particle $P(\boldsymbol{r}_1) = \phi$, independent of the position $\boldsymbol{r}_1$, and the probability $P(\boldsymbol{r}_1,\boldsymbol{r}_2)$ of finding two particles at certain two positions. The pair correlation function does only depend on the relative position $\boldsymbol{r}_1 - \boldsymbol{r}_2$ between two particles. For isotropic particles, the correlation is also isotropic, while for platelets we have to assume a preferred direction, as we will see below.

In a simple way, one can derive a structure factor for hard spheres that simply cannot overlap. One can derive the following:

$$S(Q) = 1 - \phi_{2R} \cdot F_{\text{sphere}}(Q, 2R) \approx \left(1 + \phi_{2R} \cdot F_{\text{sphere}}(Q, 2R)\right)^{-1} \tag{23}$$

In the first expression, the form amplitude of a sphere appears (eq. 9) with double the radius and a concentration according to double sized spheres, i.e. $\phi_{2R} = 2^3 \, \phi$. This takes care of the minimum distance between two spheres of radius *R*. The second expression is highly similar to the first one (same leading order for small ϕ), and results from a simple Ornstein-Zernike approach. A more detailed Ornstein-Zernike approach exists for hard spheres with a few more terms [34] – see also Appendix 10.11.

10.6.1 Structure factors for clay systems

The stacking of several clay platelets gives rise to at least one peak: The 1st order peak is directly connected to the spacing *d* of the platelets according to $d = 2\pi Q_{\text{max}}^{-1}$ (see also eq. 3). A simple experiment is described for smectite in water that was slowly heated from -70°C to room temperature [34] (Figure 6). One can see that, with increasing the temperature, the lamellar spacing increases from 15 to ca. 100Å. As long as one focuses on the first order peak position, one could stop here, but more details lie in (a) the small angle scattering, where whole stacks are observed, (b) in the peak width, and (c) in relative widths of higher order peaks. In the following, we will give several approaches that focus on the different aspects.

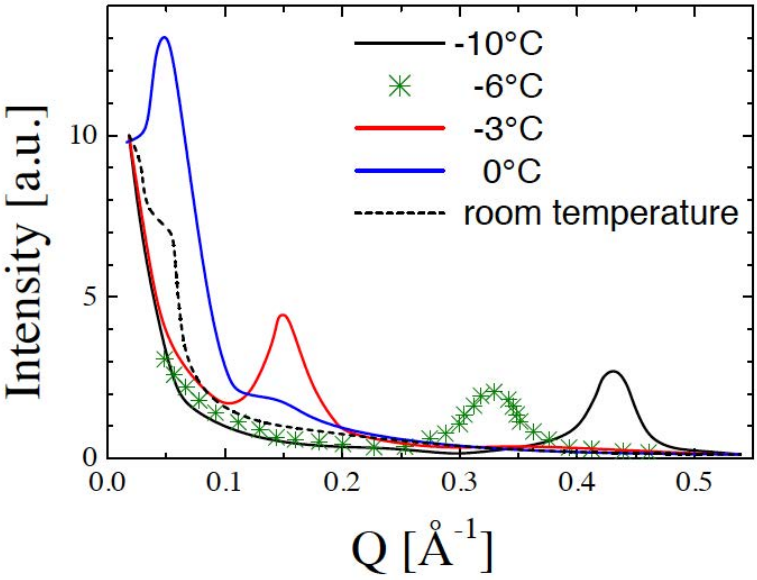

Figure 6: SAXS patterns of smectite in water that is slowly heated from **-10°C** to room temperature. Gradual swelling occurs with elevated temperatures. ~~Note that the SAXS scattering vector s is related in the following $2\pi s \equiv Q$, and $d = s^{-1}$.~~ Graph modified from Ref. [35].

For stacks of platelets, ideally with their centers on the same normal line, one would obtain the following stack form factor:

$$F^2(Q) = \int_0^{\frac{\pi}{2}} d\vartheta \, \hat{S}(Q,\vartheta) \cdot \hat{F}^2(Q,\vartheta) \sin\vartheta \tag{24}$$

We can see here an internal structure factor $\hat{S}(Q,\vartheta)$, that describes only the correlations of single platelets along the z-axis. The platelet form factor $\hat{F}^2(Q,\vartheta)$ refers to eq. 12. With this concept one would describe whole stacks that are embedded further in a matrix. The simplest internal structure factor is obtained, when all stacks have an identical number of platelets N [27]:

$$\hat{S}(c) = \frac{\sin^2(cN)}{\sin^2(c)} \tag{25}$$

with the argument $c = (Qd/2)\cos\vartheta$. For a distribution of the platelet number n with the probability being constant for all n and a maximum $n_{max} = N$, one obtains [27]:

$$\hat{S}(c) = \frac{2N - \sin(2cN + c)/\sin(c) + 1}{4N\sin^2(c)} \tag{26}$$

For a Poisson distribution of the platelet number n with the mean value <n> = λ, one obtains [27]:

$$\hat{S}(c) = \frac{1 - \cos\left(\lambda \cdot \sin(2c)\right) \cdot \exp\left(-2\lambda \sin^2 c\right)}{2\sin^2(c)} \tag{27}$$

All of these structure factors display identical Bragg peaks at Q = 0, Q_{max}, $2Q_{max}$, $3Q_{max}$, … as seen in Figure 7. The most interesting detail is the shape of the small angle scattering at small $Q < 0.1\text{Å}^{-1}$, where the statistics of the n-distribution really matters (see Figure 8). For higher Q, the resolution of neutron scattering experiments is usually such relaxed that peak shapes are not that well distinguished experimentally. The form factor that still has to be considered is responsible for the decay of the Bragg peaks at higher Q that makes higher order peaks nearly invisible for SANS. So, wide and medium angle x-ray scattering experiments are usually the better choice for observing higher order Bragg peaks and peak widths. After we have seen the theories for identical peak shapes of all orders, a few examples should be given for different peak shapes at different orders.

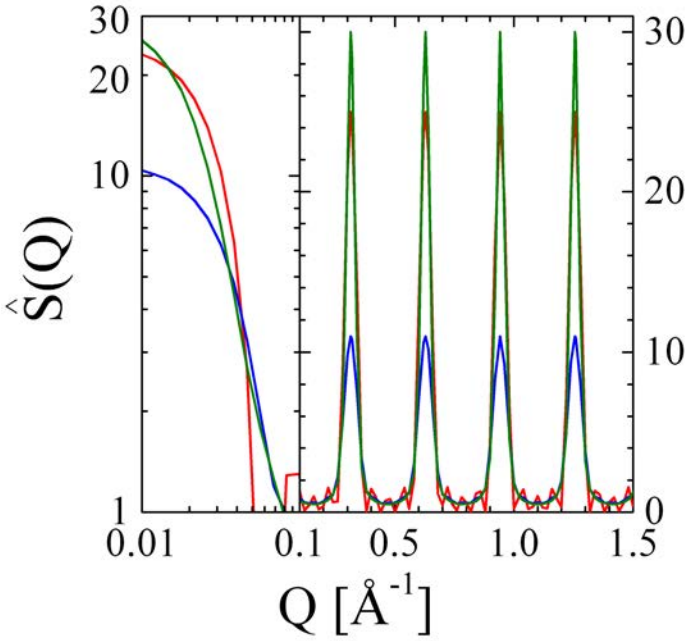

Figure 7: Structure factors for stacks with different statistics: (red) fixed number N = 5 of platelets in stack, (blue) same probability for n = 1..5 platelets in stack, and (green) Poisson distribution of n with mean value λ = 5. The spacing is 20Å. Note the log-log scale in the left section, while the scale **is** linear else.

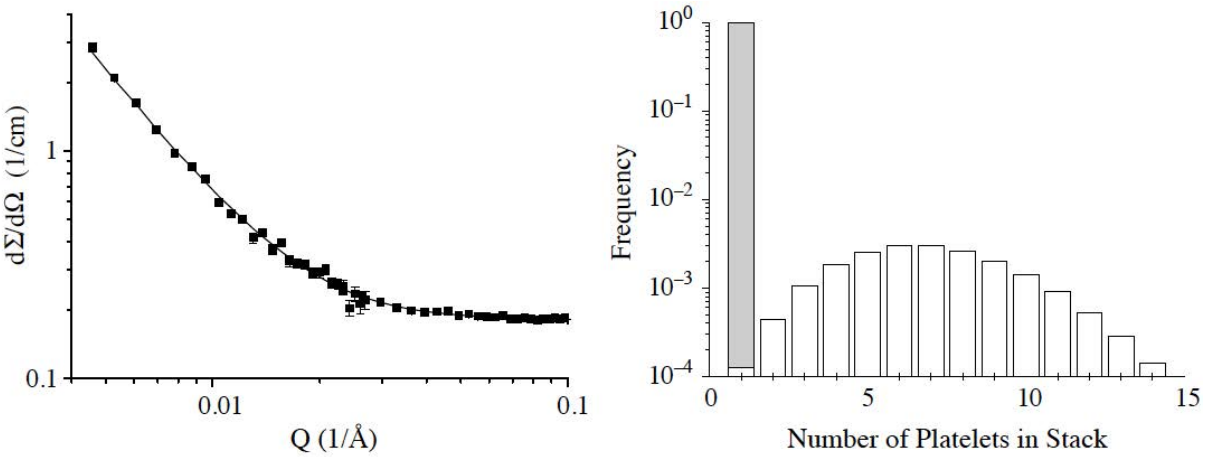

Figure 8: (left) Typical small angle neutron scattering pattern of a MMT clay in water dispersion. Even though the scattering pattern looks quite featureless, isolated platelets and a Poisson distribution for the platelet number in a stack had to be assumed (right). From Ref. [27].

For regular repetitions of identical building blocks, the theory of crystals has been developed best [13]. From the theory of crystals the following picture has been developed: For the first three structure factors, we have assumed no uncertainty of the repeat distance. This results in equally shaped Bragg peaks at all orders. In this case, only the finite size $\varnothing$ of the crystallite determines the peak width of all peaks through a correlation length $\xi \sim \varnothing$. So the neighborhood of platelets remains well defined. The second kind of uncertainty (see also [14]) is introduced, when the probability becomes wider and wider when considering neighbors at larger distances. This means, that each particle only refers to its immediate neighbor, which results in a loss of wide-range order. This scenario describes a paracrystal.

Kratky and Porod [36, 37, 38] introduced a Gaussian distribution for next-neighbor correlations, which results in wider Gaussian distributions over longer distances [2]. The expression for this structure factor reads:

$$\hat{S}(c) = 1 + \frac{2}{N}\sum_{k=1}^{N}(N-k)\cos(2kc)\exp\left(-2k\frac{\sigma^2}{d^2}c^2\right) \tag{28}$$

We see, that the total number of platelets is limited to N. The integer k describes the index difference of the platelets, which appears in the Gaussian factor. In reciprocal space the corresponding Gaussian gets narrower – contrarily to real space.

While in the abovementioned structure factor the mean distance is fixed, and, therefore, a weakly paracrystalline model, another approach for intercalated polymer/clay nanocomposites can be made: Now by d the minimum distance is described, and a simply exponential decaying potential with a decay length L describes the next neighbor interactions. Now, the potential allows for detachments and would be called “strongly paracrystalline”. The structure factor reads:

$$\hat{S}(c) = \frac{4\left(\frac{Lc}{d}\right)^2}{2 + 4\left(\frac{Lc}{d}\right)^2 - 2\cos 2c + 4\frac{Lc}{d}\sin\ 2c} \tag{29}$$

Both structure factors of the two paracrystalline models are compared in Figure 9. While the first model loses the higher order peaks quite quickly, the second model keeps higher order peaks well. This corresponds to the short distance correlations which are better in the second case. The first model still provides a description of small angle scattering at the zero order peak, while the second model leads to such a homogenous clay distribution that small angles scattering is predicted to be absent. This fact is a clear inconsistency of the second model, which does not apply in reality. The origin is the

assumption of low platelet concentrations that in reality also give rise to random orientations and therefore well distinguished stacks that do scatter at small angles.

From the first order peak width of the second model, the mean number of platelets in a stack can be calculated when comparing to eq. 25. In the limit of large platelet numbers or small L one would obtain:

$$\langle N \rangle \approx \sqrt{6\frac{\xi^2}{d^2}+1} \approx \sqrt{\frac{3}{\pi^2}\cdot\frac{d^2}{L^2}+1} \tag{30}$$

The equilibrium total spacing δ refers to the first maximum of the structure factor, and is depicted in Figure 9b. The distance distribution function can be motivated by the minimum distance d that is at least the platelet thickness, and the parameter L that can be explained through a chemical potential μ: If the polymer deformation is assumed to be in the normal direction, the potential would read $\mu = k_B T\,(1-\Delta^2/R_g^2) \approx k_B T$. For strong deformations, the detail about the exact deformation is lost. In the comparisons with literature data below, the actual chemical potential seems to be smaller than estimated here. For conceptual reasons we leave the explanation as it is. The number of polymers between two platelets is given by $n = \pi R^2 \Delta \,/\, V_m$, where R is the platelet radius, and Δ the spacing between the platelets. Now, the distribution function for the spacing would read $\Psi(\Delta) \sim \exp(-(\mu/k_B T)\pi R^2 \Delta / V_m)$, and so

$$L = \frac{V_m}{\pi R^2 \mu / k_B T} \tag{31}$$

For the stacking number <N> one would expect a decaying dependence with the molar polymer volume V_m [39], while the spacing would increase [40]. The two literature examples [39, 40] are only semi-quantitatively representing the described dependencies here, but the observed trends are correct. The presented model is the simplest attempt to explain the connections between different parameters of intercalated polymer/clay systems for non-grafted polymers at low particle concentrations.

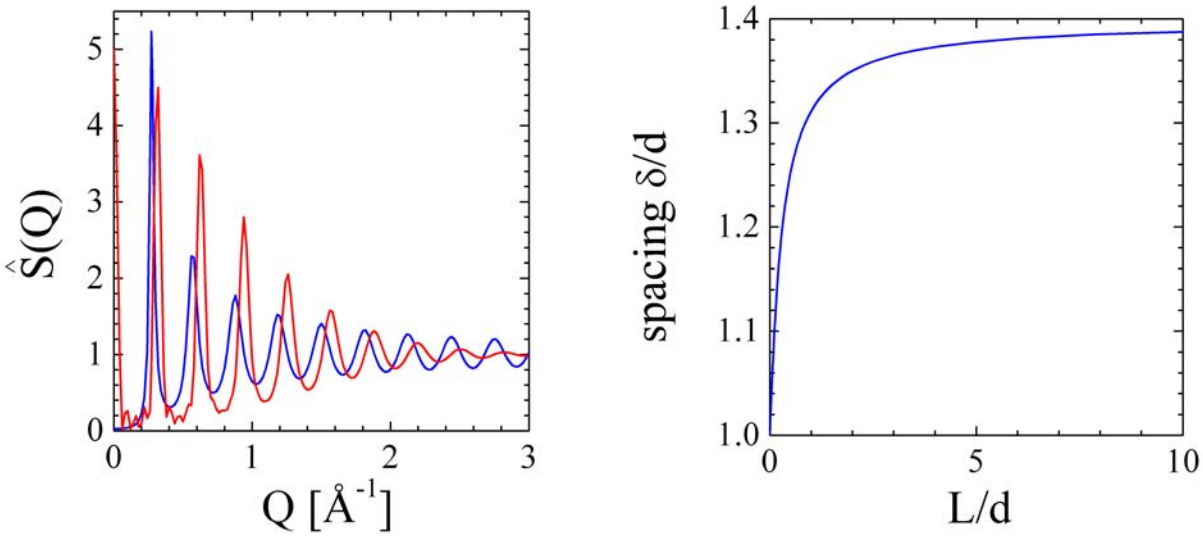

Figure 9: (left) Comparison of the structure factors of paracrystalline models (d = 20Å). The red curve corresponds to the Kratky-Porod model (N = 5) with Gaussian distributions of the distortions (σ = 1Å), while the second model assumes an exponential decay (L = 3.9Å → <N> = 3) of the next neighbor distance distribution. (right) the spacing of the second model as a function of the scaled L parameter.

Some experimental results about rubber filled clay systems are depicted in Figure 10 [41]. The pure clay shows sharp peaks that weakly decay in intensity, which indicates high degree of order. The intercalated systems show a much faster decay of higher order peaks which might be addressed to a paracrystal structure. At very high clay contents the spacing seems to be dominated by the average space that a clay sheet has.

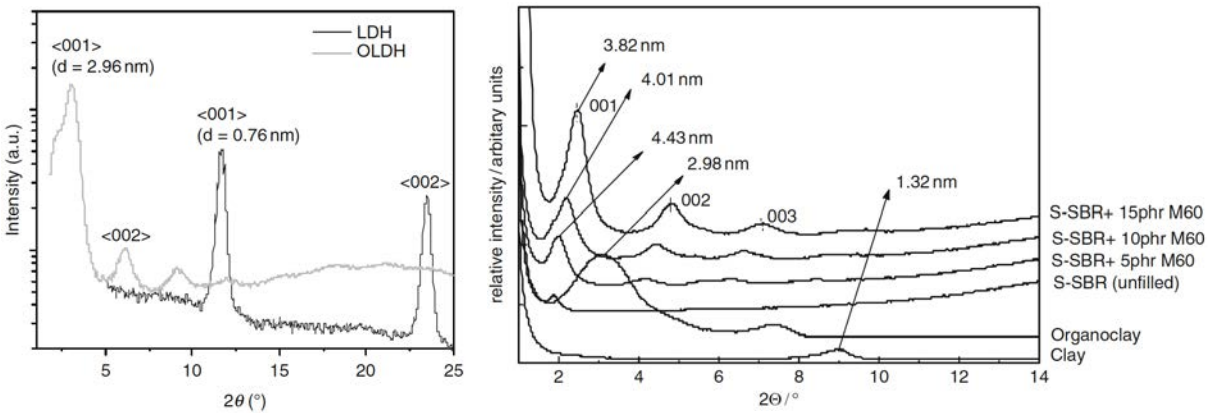

Figure 10: (left) The influence of rubber intercalation to LDH clay. The pure clay shows highly ordered stacks, while the intercalated system has clear indications for disorder that likely is a paracrystal structure. (right) The influence of high organo-clay (M60) contents on styrene-butadiene rubbers (S-SBR) in units of *phr* (per hundred rubber). The high clay contents seem to equally distribute such that the spacing reduces. From Ref. [41].

The focus on the structure factor distracted from the presence of the form factor. For small stacking numbers (i.e. <N> d << R) the form factor is present, and would appear as follows due to the separation of length scales:

$$F^2(Q) = \frac{2}{Q^2R^2} \cdot \left(1 - \frac{J_1(2QR)}{QR}\right) \cdot \frac{\sin^2(QH)}{Q^2H^2} \cdot \hat{S}(c = Qd/2) \tag{32}$$

Practically, the first term ~Q^{-2} is essential in the WAXS patterns, and the single platelet thickness $H = d/2$ might appear as well. Note that for pure clay the stack thickness is so high, that the form factor can be assumed to be constant. Intermediate stacking numbers require the full orientational averaging as of eq. 24.

10.7 Polymer Scattering

Since polymers are one main material that is used for intercalation and exfoliation, many studies aim at the chain structure of polymers. As already intuitively clear, the chains can be rather undisturbed at low particle concentrations far apart from the platelets, and strongly deformed in the intercalated state between the platelets. Interestingly for

spherical colloids, most of the polymers stay rather unchanged in the presence of the particles – even at higher particle concentrations [42]. For simplicity and clarity we start with the concepts of undeformed chains, and then end at deformed intercalated chains [14, 15].

The scattering function of a random coil for a chain was first derived by Debye. Using the statistics of a random walk, one obtains the Debye function:

$$F^2(Q,f) = \frac{2}{Q^4 R_g^4} \cdot \left(\exp\left(-f \cdot Q^2 R_g^2\right) - 1 + f \cdot Q^2 R_g^2\right) \tag{33}$$

For later expressions we introduced a segment fraction f of the overall chain. For simple homopolymers we set $f = 1$, and obtain the full Q-dependence of the scattering in the case of non-interacting chains. The polymer size is given in terms of the radius of gyration R_g. The neglect of interactions is true in theta-solvents [43] and nearly true in melts of polymers with different hydrogen isotope labeling [44]. The theoretical and experimental dependencies are depicted in Figure 11. The Guinier scattering at small Q and the fractal structure of coils at high Q can be analyzed further [45, 46], but would take us far from the scope of this manuscript. For the absolute scattering of non-interacting polymers of the same polymerization degree one obtains then:

$$\frac{d\Sigma}{d\Omega}(Q) = (\Delta\varrho)^2 \cdot \phi \cdot (1-\phi) \cdot V_{\text{polymer}} \cdot F^2(Q,1) \tag{34}$$

We have already seen the general dependence in eq. 8, but now the labeled polymer fraction ϕ can be high. This new expression results from the random phase approximation (RPA) that describes concentrated systems [15] and that will be derived in the following. Here, we mainly restrict ourselves to polymer systems. The basis of the RPA is the matrix of the undisturbed polymers. In the case of well distinguished homopolymers, the matrix is diagonal:

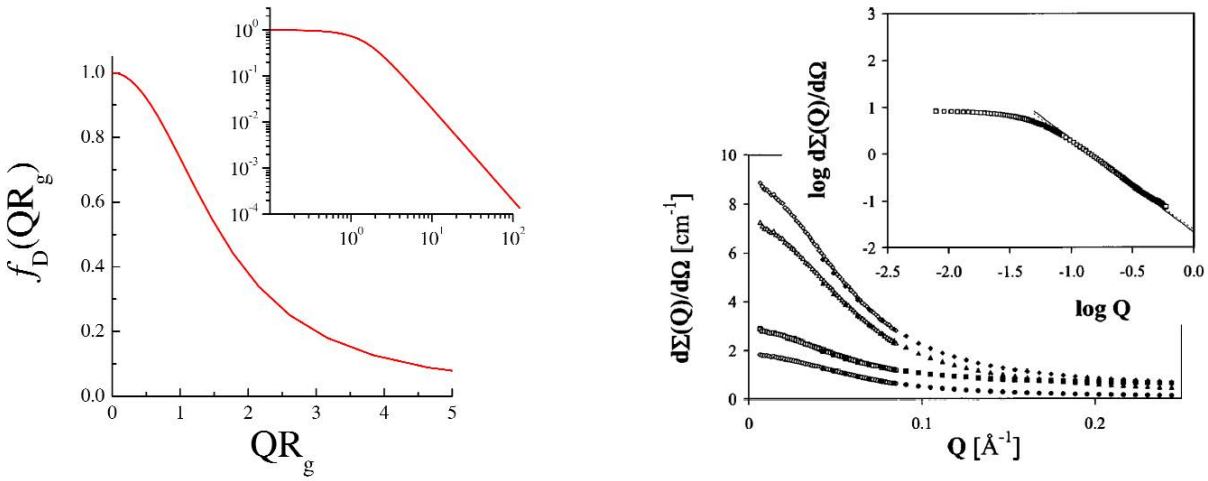

Figure 11: (left) The theoretical Debye function in a linear and double-logarithmic plot. (right) The experimental scattering of a homopolymer melt of protonated and deuterated chains, again linear and double-logarithmic. From Refs. [44, 46]

$$\boldsymbol{S}_0(Q) = \begin{pmatrix} \phi_1 V_1 F_1^2 & 0 & 0 \\ 0 & \ddots & 0 \\ 0 & 0 & \phi_n V_n F_n^2 \end{pmatrix} \tag{35}$$

In the case of diblock copolymers (i.e. linear chains with two different monomers, block-wise distributed along the chain), off-diagonal entries appear in the matrix. In the case of a simple diblock copolymer melt, one obtains the following matrix [47]:

$$\boldsymbol{S}_0(Q) = \phi V \begin{pmatrix} F^2(Q,f) & \frac{1}{2}(F^2(Q,1) - F^2(Q,f) - F^2(Q,1-f)) \\ \frac{1}{2}(F^2(Q,1) - F^2(Q,f) - F^2(Q,1-f)) & F^2(Q,1-f) \end{pmatrix} \tag{36}$$

From this concept, it is possible to build an N×N matrix for any kind of polymers with N kinds of well separated polymeric blocks. If a one-phase system is assumed, the entries for the same kind of monomers can be compressed in terms of a simple addition (i.e. $S_{kk}^{\text{eff}} = \sum_{i\in\{k\}} S_{ii}$ and $S_{kl}^{\text{eff}} = \sum_{i\in\{k\},j\in\{l\},i>j} S_{ij}$ for $k > l$ and correspondingly for $k < l$). All of this yielded the correlation matrix of unperturbed chains. For interacting polymers, a second matrix describes the monomer-monomer interactions:

$$\boldsymbol{V} = \begin{pmatrix} v_{11} & v_{12} & \cdots & v_{1n} \\ v_{21} & v_{22} & \cdots & v_{2n} \\ \vdots & \vdots & \ddots & \vdots \\ v_{n1} & v_{n2} & \cdots & v_{nn} \end{pmatrix} = \begin{pmatrix} v & v-\chi_{12} & \cdots & v-\chi_{1n} \\ v-\chi_{12} & v & \cdots & v-\chi_{2n} \\ \vdots & \vdots & \ddots & \vdots \\ v-\chi_{1n} & v-\chi_{2n} & \cdots & v \end{pmatrix} \tag{37}$$

The first expression leaves much space for specific interactions, but usually the parameters can be reduced by introducing a strong repulsive parameter v that is basically the same for all monomers, and a specific exchange interaction χ_{ij} that describes the energetic change of i-i and j-j contacts by i-j contacts. Practically, for most polymer systems the interactions are point-like, and therefore Q-independent. The central correlation function including interactions is then expressed by

$$\boldsymbol{S} = (\boldsymbol{S}_0^{-1} + \boldsymbol{V})^{-1} \tag{38}$$

This expression is still a matrix that cannot simply be compared to a simple scattering experiment. The key is the scattering contrasts, that have to be considered for each monomeric species:

$$\boldsymbol{\varrho} = \begin{pmatrix} \varrho_1 - \varrho_x \\ \vdots \\ \varrho_n - \varrho_x \end{pmatrix} \tag{39}$$

Here, the contrast vector introduces an arbitrary reference scattering length density ρ_x that can be picked from any species. This step is exactly valid in the limit of incompressibility, which is well respected for most systems. The overall scattering function then reads:

$$\frac{d\Sigma}{d\Omega}(Q) = \lim_{v\to\infty}(\boldsymbol{\varrho}^{\mathrm{tr}}\boldsymbol{S}\,\boldsymbol{\varrho}) \tag{40}$$

The incompressibility limit of the model is achieved by leaving the repulsive interaction go to infinite values. This formalism was applied to many simple systems. In the case of a homopolymer blend with two arbitrary polymers one obtains:

$$\frac{d\Sigma}{d\Omega}(Q) = (\Delta\varrho)^2 \cdot \left(\frac{1}{\phi_1 V_1 F_1^2(Q,1)} + \frac{1}{\phi_2 V_2 F_2^2(Q,1)} - 2\chi_{12}\right)^{-1} \tag{41}$$

The volume fractions ϕ_i and molar volumes V_i refer to species *i*. As seen from the dimensions, the interaction parameter χ_{12} has the unit of a reciprocal volume. It can be seen as a dimensionless interaction parameter $\tilde{\chi}$ divided by the monomeric volume, i.e.

$$\chi = \tilde{\chi}/v_0 \tag{42}$$

This concept was derived for polymer chains with a small perturbation through the monomer-monomer interactions. It proved to be highly successful for many kinds of polymer blends with even more than 2 kinds of monomers [48]. And even colloidal particles could be introduced to this formalism [49].

The briefly mentioned option of changing contrast is ideally possible for neutron scattering experiments by exchanging hydrogen through deuterium for polymers (or solvents). In this way, specific aspects of the sample can be highlighted. Reference 50 presents a thorough study to obtain the pure polymer scattering in a nanocomposite with spherical silica filler [4]. There, the single polymer was replaced by a mixture of hydrogenous and deuterated polymer that on average possesses the same scattering length density of the particles. Apart from being successful, the preferential absorption of one of the labeled polymers caused slight complications that still could be modeled well.

The general approximated approach of the RPA can be understood on two levels: First, the fluctuations of the polymer concentration that give rise to the scattering as described above cannot exceed the local concentration of 0 or 1. The RPA would predict such unreasonable strong fluctuations close to phase boundaries, where the system tends to separation anyhow. Second, the strong fluctuations have an impact on the Free Energy of the system that is neglected by the RPA, which explains where the simplification would need to be corrected. Reference 51 gives a brief overview on critical fluctuations of homopolymer blends and of diblock copolymers. Historically, Schwahn emphasized this topic for homopolymer blends [52], that then was observed for diblock copolymers by several groups, and finally conceptually taken to mixtures of two homopolymers and a corresponding diblock copolymer [53,54] for instance. While the concepts have been rather well understood, they were widely neglected in polymer/particle nanocomposites. But the attractive Casimir force, for instance, is discussed for binary liquids [55] and polymer solutions [34] so far, and detailed considerations for polymers are about to be developed [56].

10.7.1 Confined polymers

For chains that are confined between clay platelets other formalisms were introduced. The ideal case of a polymeric monolayer results in self-avoiding trails discussed by Duplantier [57]. For slightly thicker layers of polymers, the partially self-avoiding trails model the experimental behavior. This is often true, because the minimum polymer layer thickness is ca. 10Å, which leaves space for 2-4 chains in the normal direction. The resulting scattering function reads:

$$S(Q) = \frac{1}{v_0} \cdot \left(1 + \frac{Q^2 \xi_0^2}{1 + \kappa \ln \frac{K}{Q^2 \xi_0^2}} \right)^{-1} \tag{43}$$

The classical correlation length $\xi_0 = a_0/\sqrt{v_0 c_0/2}$ appears already for the random phase approximation without corrections. The logarithmic correction depends on the Ginzburg number $\kappa = (4\pi c_0 a_0^2)^{-1}$, and a less well determined constant K of order 1. The magnitudes v_0, c_0, and a_0 are the 2-dimensional interaction parameter, the monomer concentration, and the statistical segment length (divided by the number $\sqrt{2d} = 2$), respectively. The concentration and the interaction parameter are connected to the 3-dimensional counterparts by $c_0 \sim c_{3d}H$, $v_0 \sim v_{3d}/H$, where H is the thickness of the polymer layer. The interaction parameter v_0 is normalized in a way that it takes zero at the critical point (or spinodal) and, therefore, can also be seen as a reduced temperature $v_0 \sim (T - T_0)^{\gamma}$ with the critical exponent γ.

The experimental thrill was to remove the unwanted scattering of the clay particles from the polymer scattering [58]. So the polymer scattering was rendered high by using hydrogenous and deuterated polymers, and the still high clay background was determined in a polymer concentration series. The rather pure polymer scattering is depicted in Figure 12. One can see that the model describes the scattering well for smaller $Q < 0.04$Å^{-1}, to which the model applies. All fitting parameters are given in reference [58]. The cross-check of this model was obtained by comparing the fitted Ginzburg number κ with the independently calculated κ that was obtained from the other fitting parameters. Astonishingly, the agreement was within a few percent for the LRD80 clay particles with a diameter of 80nm, but discrepancies were observed for the smaller clay diameter of 20nm. The explanation was the polymer dimension in the lateral direction: Still several polymers were placed on the LRD80 platelets, while the number of polymers was too small for LRD20, where an additional confinement might occur through the finite diameter.

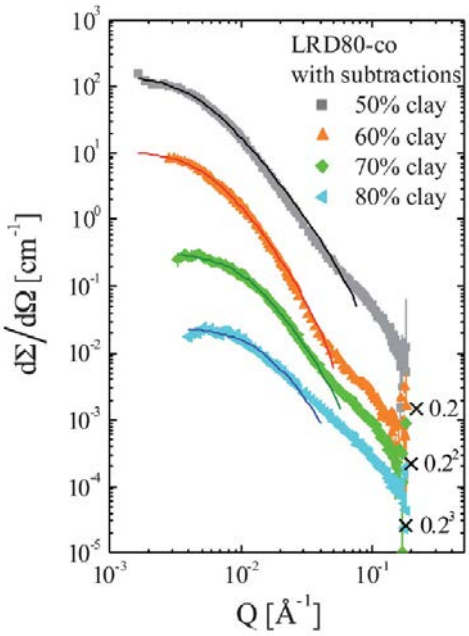

Figure 12: The polymer scattering of 2-dimensional h- and d-PEO polymers between clay platelets LRD80 at different clay concentrations. The model fits correspond to eq. 43. The downturn of the fits towards higher Q at ca. 0.04Å^{-1} corresponds to the limit of the model where the logarithm turns negative. From Ref. [58].

10.8 Contrast Variation.

The basic understanding of experiments with varying contrasts would already be clear in context of the two equations 39 and 40 (the incompressibility limit applies, but does not need to be mentioned explicitely). The experiment would change at least one contrast over a wider range such that one species becomes invisible at the contrast match point. For two different materials one can obtain the experimental scattering length density. This is for instance important for natural materials such as clays, while the solvent scattering length density can be calculated on the basis of the changing deuterium to hydrogen ratio. Apart from the experimental match point, one observes the residual scattering that results from inhomogeneities within the particles. For clay particles there occur inhomogeneities in the lateral direction due to changing counter ions and possibly wrinkles [27].

These inhomogeneities are also highly important for particles consisting of two materials. At the overall match point the forward scattering is widely reduced, and the internal structure remains. Apart from that, a single material can be made invisible at the particular match point, and the other material structure is observed as a pure structure. By this kind of experiment, a more detailed picture is obtained that distinguishes between the two materials of the particle [59].

In multidimensional contrast variation experiments, the match points of each individual species should be selected in several series of experiments [21]. This highlights separately different aspects of the complicated structure, and the individual aspect can be recovered from the whole set of experiments. Formally, the equation 40 includes several sets of contrasts. If the contrast matrix were quadratic, one could solve for the correlation matrix exactly. To reduce the noise of this procedure, one better over-

determines the problem by performing more measurements than actually needed, and then a formal inverse matrix for $\boldsymbol{\rho}$ can be calculated by the singular value decomposition method. The result of this experiment are the isolated structures on the diagonal of $\boldsymbol{S}$, and the cross-correlations that tell about the relative positions of different species. While a single scattering experiment has to deal with the phase problem, that makes it impossible to determine the real space structure exactly, the multidimensional contrast variation experiment overcomes parts of this phase problem – at least in terms of the different species.

10.9 Resolution and Size Distribution

A particular problem of scattering experiments shall be addressed briefly here. Many theories predict fringes of the scattering pattern at higher Q, while experimentally the curves are smeared [60]. This simplifies the analysis of power laws, but reduces the exactness of a size measurement. The instrumental resolution arises from a wavelength spread and a finite collimation. Often, the connection between a theoretical scattering function (index th) and an experimental one (index exp) is given by

$$\frac{d\Sigma_{\mathrm{exp}}}{d\Omega}(Q_{\mathrm{av}}) = \frac{1}{\Delta Q\sqrt{\pi}} \cdot \int dQ \, \frac{d\Sigma_{\mathrm{th}}}{d\Omega}(Q) \cdot \exp\left(-\frac{(Q - Q_{\mathrm{av}})^2}{(\Delta Q)^2}\right) \tag{44}$$

using the particular spread ΔQ in terms of Q. While for SANS this spread is in itself Q-dependent, for x-ray scattering the resolution effect is often negligible. Here, the sample polydispersity comes into play: Often single or multiple lengths in the sample structure are distributed. They would also be described by a smearing, according to:

$$\frac{d\Sigma_{\mathrm{distr}}}{d\Omega}(Q, \ell_{\mathrm{av}}) = \frac{1}{\Delta\ell\sqrt{\pi}} \cdot \int d\ell \, \frac{d\Sigma_{\mathrm{mon}}}{d\Omega}(Q, \ell) \cdot \exp\left(-\frac{(\ell - \ell_{\mathrm{av}})^2}{(\Delta\ell)^2}\right) \tag{45}$$

The monodisperse scattering function (index mon) is smeared over the parameter ℓ to yield the scattering function of a distribution (index distr). The smearing parameter is $\Delta\ell$. The two different origins of smearing are identical in the case that both focus on the same length scale, i.e. $Q_{\mathrm{av}} = 2\pi/\ell_{\mathrm{av}}$. The simple exponential distribution can also be replaced by a Schultz-Zimm distribution [49].

10.9 Dynamics in complex fluids containing clay particles

In the former sections we have introduced already most of the important length scales and discussed the static structure factor, which are typically measured by means of the SANS technique. The accessible length scales of SANS lie in the range of 1 to 100 and even 1000nm. Small Angle X-ray Scattering (SAXS) is an interesting alternative but most applicable for the particle-like scattering due to the contrast definition in terms of electron density differences like clay, but not for detailed polymer scattering. However, scattering experiments in general allow for resolving dynamics of the sample, when the energy change of the probe (neutron or photon) is considered. In most cases of Soft Matter research, the typical energies of neutrons are much more suitable for this kind of

experiments compared to x-rays. Especially for the long length scales of several nm to 100nm, the method Neutron Spin Echo (NSE) spectroscopy involves Fourier times of up to 0.7µs [62]. So, this quasi-elastic scattering method resolves energies of µeV to neV on the same length scales as SANS.

The general view on elastic scattering goes back to a more elementary view, where energy and momentum transfers are observed, i.e.:

$$\Delta E = \hbar\omega = E_i - E_f \tag{46}$$

$$\Delta p = \hbar Q = \hbar\left(k_i - k_f\right) \tag{47}$$

The suffixes *i* and *f* refer to the initial and final stages. The method of small angle scattering neglects the energy transfers, because they barely change the momentum balance, while NSE spectroscopy manages to resolve tiniest energetic changes. The most important elementary scattering contribution is the coherent scattering:

$$S_{\mathrm{coh}}(Q,t) = \frac{1}{N}\langle \sum_{j,l=1}^{N} \exp\left(i\boldsymbol{Q}\left(\boldsymbol{r_j}(t=0) - \boldsymbol{r}_l(t)\right)\right)\rangle \tag{48}$$

similarly to Eq. 5. The coherent scattering contribution measures time-dependent correlations between the same species against the matrix. For the time t = 0, the classical SANS formula is obtained (Eq. 5). The focus of the coherent scattering is the movement of the whole matter of species A against the matrix, and so individual 'atoms' do not matter. For completeness, the incoherent scattering focuses on the same 'atom' in the sense of the abovementioned formula 48 with *j* = *l*. Here, the individual 'atoms' matter, and for instance the exchange of the same species would contribute to the scattering signal.

As formulated in Eq. 48, the thermodynamic average <…> leads to a symmetric scattering contribution $S_{\mathrm{coh}}(Q,t) = S_{\mathrm{coh}}(Q,-t)$, because the formation of fluctuations is symmetric to their decay. Even for non-equilibrium systems, the NSE method would symmetrize the scattering signal according to $S_{\mathrm{NSE}}(Q,t) = \frac{1}{2}(S_{\mathrm{coh}}(Q,t) + S_{\mathrm{coh}}(Q,-t))$, which would matter in flow experiments for example.

The first example that is discussed here deals with rather diluted polyethylene oxide (PEO) polymers and clay particles dispersed in water [61]. This system can be seen as an intermediate state for the preparation of PEO/clay nanocomposites by solvent casting. This route was actually taken in the example above (chapter 10.7.1) where the aim was the polymer scattering. In the current case the polymer was fully hydrogenous, while heavy water introduced the contrast to both clay and polymer. Using neutron spin echo spectroscopy, the relaxation of the thermal fluctuations is observed. In our case we described these relaxations by a stretched exponential function (from the Kohlrausch-William-Watts theory [63]) and an elastic background:

$$\frac{S(Q,\tau)}{S(Q,0)} = (1 - f_{\text{el}}) \exp\left[-(\Gamma\tau)^{\beta}\right] + f_{\text{el}} \tag{49}$$

The elastic background f_{el} takes care of the immobile clay scattering (on the nanosecond time scale). The relaxation rate Γ describes the typical speed of the system at the observed scattering angle Q, and the positive stretch exponent β is closer to 1 for diffusive motions and lower for more confined motions. Experimental NSE curves of system are depicted in Figure 13 together with the fitted curves of equation 46. One can directly see, that at smaller scattering vectors Q the elastic contributions are higher while they are lower at higher Q. This elastic contribution f_{el} is depicted in Figure 14 as a function of the scattering vector Q. The function is decaying with increasing Q. This means that at small Q the spatial window around the clay particles is large such that motions are only observed between the static window and the outside. The fraction of polymers outside the window is small for large windows, but with increasing Q the fraction becomes bigger. The solid line in Fig. 14 corresponds to a Lorentzian curve with the typical width Ξ = 9Å that is connected to the polymer structure thickness, and is called localization length. Within the dynamic interpretation this thickness is obtained quite naturally, while for pure SANS experiments this structure had to be determined by a series of different polymer contrasts, which were quite a chemical synthesis effort. So, using NSE we could determine the adsorbed polymer structure on clay platelets, while SANS with contrast variation delivers similar results [64].

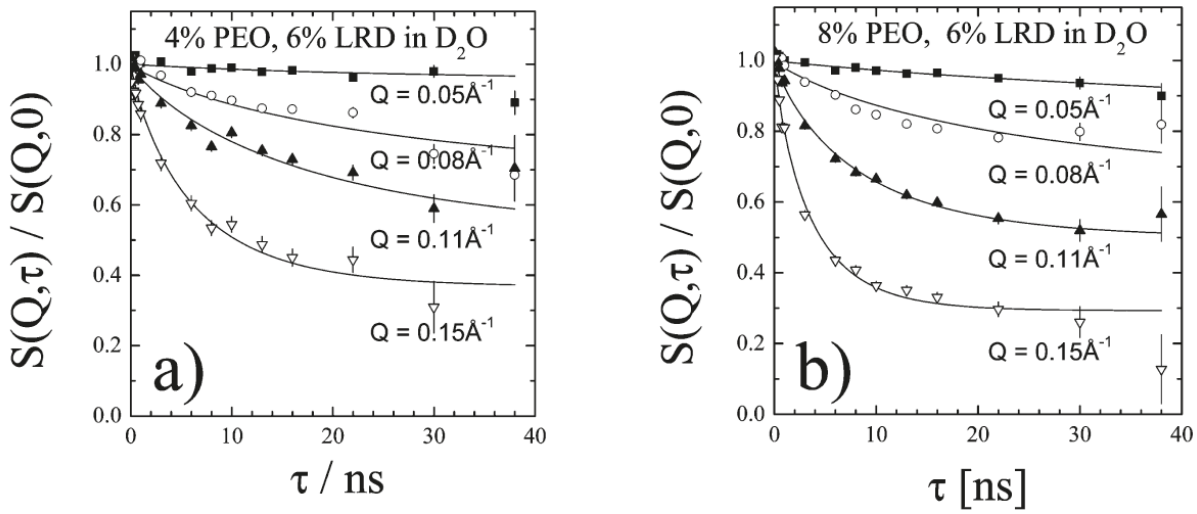

Figure 13: Experimental NSE relaxation curves for different scattering vectors Q, and different polymer concentrations [(a) 4% PEO and (b) 8% PEO]. The solid lines are fit curves with a stretched exponential and an elastic contribution, according to eq. 49. From Ref. [61].

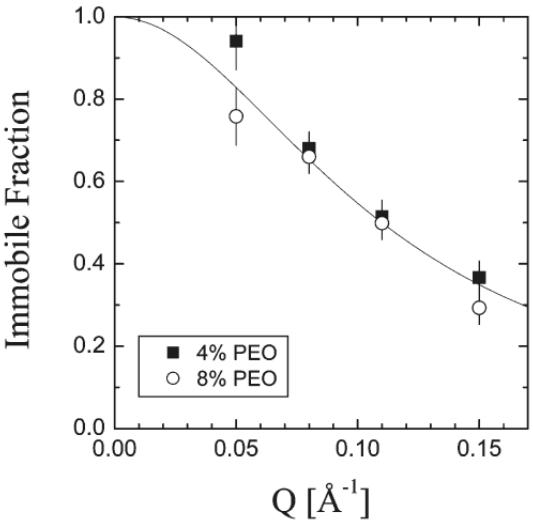

Figure 14: The elastic contribution f_{el} as a function of the scattering vector Q. This curve is described by a Lorentzian with the width Ξ, the localization length, describing the polymer thickness around the clay particles. From Ref. [61].

Another system introduces microemulsions as complex fluids to which the clay particles are introduced. Microemulsions consist of oil, water and a surfactant [65]. On the nano-scale, domains of well-separated oil and water are found. The surfactant mediates between the two phases and is found as a film between them, such that the microemulsion appears macroscopically homogenous. For equal amounts of oil and water, the bicontinuous structure is found: Both domains are continuous sponge structures that host the other one, such that on macroscopic length scales domains are still connected. The latter property can be proven by conductivity measurements or NMR [66].

Planar hydrophilic surfaces lead to an ordering of the microemulsion: A few perfect lamellar domains form in the vicinity of the surface, before perforations induce a continuous loss of the order towards the bulk, where the microemulsion is still bicontinuous. Such surfaces can be introduced by clay particles. Rather large particles (Nanofil) of 500nm diameter result in a well-developed order of the microemulsion, such that the two typical time scales of the lamellar structure τ_{lam} and the bicontinuous structure τ_{bic} superimpose for the clay system to form an average τ_{clay}. The ratio R_τ is defined through τ_{clay}/τ_{bic}, which is depicted in Figure 15 as a function of the clay content for different scattering vectors Q. For higher clay contents a clear deviation can be observed, and for knowing τ_{lam} the fraction f of the lamellar region within the whole system can be calculated (Figure 16). This volume fraction agrees very well with independent measurements of the thickness of the lamellar region at macroscopic planar hydrophilic surfaces (ca. 400Å on one side). The scientific field of dynamics of complex fluids at planar surfaces and specifically by introducing clay particles has to be seen in context with the rheology of complex fluids. While NSE measures the nano-scale relaxation times of the fluid, the same speed is important for the rheology of the fluid on macroscopic length scales. From this knowledge a deeper insight of surface effects is to be expected in the near future.

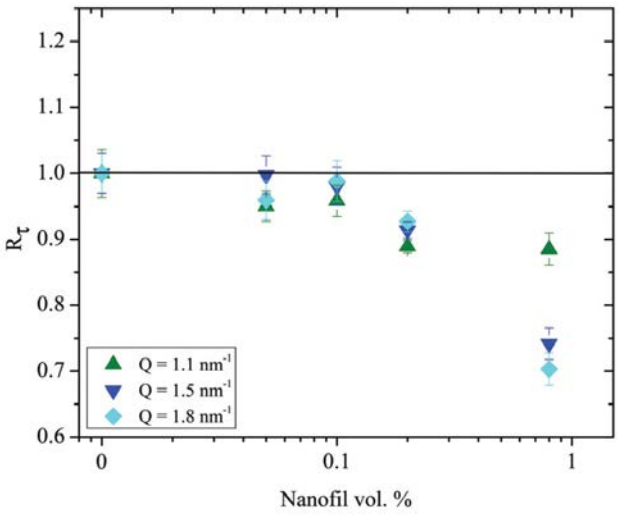

Figure 15: The ratio R_τ of relaxation times with respect to the slower bicontinuous microemulsion. For higher clay contents a clear acceleration of the averaged time is observed. From Ref. [65]

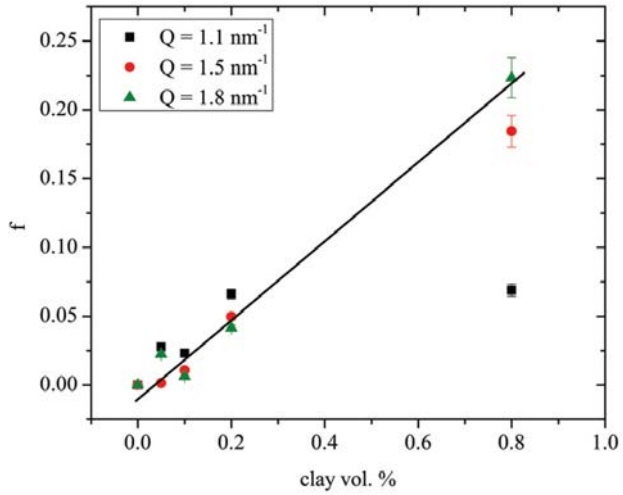

Figure 16: The fraction of the lamellar region within the whole system as obtained from the relaxation time ratio R_τ. The volume fraction of the lamellar region agrees very well with independent measurements at macroscopic planar hydrophilic surfaces. From Ref. [65].

10.10 Summary

We have seen that scattering experiments using neutrons and x-rays resolve the structure of clay systems on the important nano-scale where the microscopic understanding of macroscopic phenomena is obtained. While WAXS experiments already start at the atomistic length scale, the slightly smaller angles resolve the stacking properties of clay particles in terms of periodicity and regularity. This knowledge is highly relevant to judge about the dispersion state and the connection of macroscopic properties. Small angle scattering experiments (SANS and SAXS) finally look at length scales of 1nm to 300nm and possibly larger. Here large aggregates are observed and can also be connected to stacking properties. Again, relations to macroscopic properties are obtained. Finally, the dynamics of clay systems allows for structural analysis, but now with more details that also have an impact on the macroscopic rheology.

We have shown quite different models that allow for the quantitative interpretation of scattering experiments. We hope that the various examples and models will attract and extend the attention of scattering experiments, because the connection and understanding of microscopic mechanisms with macroscopic behavior is still on the way of improvement. Only then, the next generation of products using clay particles will be made accessible in an educated and directed way.

10.11 Appendix

The Perkus-Yevick structure factor for hard spheres is usually written [34] in terms of

$$\begin{aligned}\varrho C_{\mathrm{HS}}(Q) = -\frac{24\phi}{(\sigma Q)^6}\Big\{&\alpha(\sigma Q)^3[\sin(\sigma Q) - \sigma Q\cos(\sigma Q)]\\ &+\beta(\sigma Q)^2[2\sigma Q\sin(\sigma Q) - (\sigma^2Q^2-2)\cos(\sigma Q) - 2]\\ &+\frac{1}{2}\phi\alpha[(4(\sigma Q)^3 - 24\sigma Q)\sin(\sigma Q) - ((\sigma Q)^4 - 12(\sigma Q)^2\\ &+24)\cos(\sigma Q) + 24]\Big\}\end{aligned} \tag{50}$$

with the coefficients

$$\begin{aligned}\alpha &= \big((1+2\phi)^2 + \phi^3(\phi-4)\big)/(1-\phi)^4\\ \beta &= -\tfrac{1}{3}\phi(18 + 20\phi - 12\phi^2 + \phi^4)/(1-\phi)^4\end{aligned} \tag{51}$$

that then is combined for the structure factor:

$$S(Q) = \frac{1}{1 - \varrho C_{HS}(Q) - \varrho C_{\mathrm{attr}}(Q)} \tag{52}$$

While eqs. 50-52 describe the pure hard sphere interaction, an attractive parabolic potential of depth $\hat{A}$ between the radial coordinates σ and σ+*2R* [67] would contribute to corrections of the hard sphere structure factor by:

$$\begin{aligned}\varrho S_{\mathrm{attr}}(Q) = \frac{96\phi A}{(1-\lambda)^2(\sigma Q)^5}\big\{&(4\lambda-2)\sigma Q\cos(\lambda\sigma Q)\\ &+(\lambda(\lambda-2)(\sigma Q)^2 - 6)\sin(\lambda\sigma Q) + (2\lambda-4)\sigma Q\cos(\sigma Q)\\ &+\big((\lambda-1)(\sigma Q)^2 + 6\big)\sin(\sigma Q)\big\}\end{aligned} \tag{53}$$

with the energy parameter $A = \hat{A}/(k_{\mathrm{B}}T)$ and the relative dimension $\lambda = 1 + 2R/\sigma$. This potential can be used to mimic any short-range attraction.

References

[1] K.I. Winey, R. A. Vaia, MRS Bulletin 32 (2007) 314-322
[2] J. Oberdisse, W. Pyckhout-Hintzen, E. Straube, Structure Determination of Polymer Nanocomposites by Small-Angle Scattering, in S. Thomas, G.E. Zaikov, S.V. Valsaraj (Eds.), Recent Advances in Polymer Nanocomposites, Koninklijke Brill NV, Leiden, Boston 2009, pp. 397-438
[3] N. Cohaut, D. Tchoubar, Small-Angle Scattering Techniques, in F. Bergaya, B.K.G. Theng, G. Lagaly (Eds.), Handbook of Clay Science, Volume 5, Part B, Chapter 2.6, Elsevier, Oxford, 2013, pp. 177-211
[4] A.-C. Genix, J. Oberdisse, Curr. Opin. Coll. Interf. Sci. 20 (2015) 293-303
[5] D. L. Hunter, K.W. Kamena, D.R. Paul, MRS Bulletin 32 (2007) 323-327
[6] M. Kawasumi, J. Polym. Sci. Part A: Polym. Chem. 42 (2004) 819-824
[7] F. Bergaya, C. Detellier, J.-F. Lambert, G. Lagaly, Introduction to Clay-Polymer Nanocomposites (CPN), in F. Bergaya, B.K.G. Theng, G. Lagaly (Eds.), Handbook of Clay Science, Volume 5, Part A, Chapter 13.0, Elsevier, Oxford, 2013, pp. 655-677
[8] X. He, J. Yang, L. Zhu, B. Wang, G. Sun, P. Lv, I.Y. P, T. Liu, J. Appl. Polym. Sci. 102 (2006) 542-549
[9] G. Raos, M. Moreno, S. Elli, Macromolecules 39 (2006) 6744-6751
[10] G. Choudalakis, A.D. Gotsis, Europ. Polym. J. 45 (2009) 967–984
[11] R. Krishnamoorti, MRS Bulletin 32 (2007) 341-347
[12] L.S. Schadler, S.K. Kumar, B.C. Benicewicz, S.L. Lewis, S.E. Harton, MRS Bulletin 32 (2007) 335-340
[13] R. Hosemann, S.N. Bagchi, Direct Analysis of Diffraction by Matter, North-Holland Publishing Company, Amsterdam 1962
[14] R.-J. Roe, Methods of X-ray and Neutron Scattering in Polymer Science, Oxford University Press, New York, Oxford 2000
[15] J.S. Higgins, H.C. Benoît, Polymers and Neutron Scattering, Clarendon Press, Oxford 1994
[16] J. Viell, H. Inouye, N.K. Szekely, H. Frielinghaus, C. Marks, Y. Wang, N. Anders, A.C. Spiess, L. Makowski, Biotechnology for Biofuels 9:7 (2016) 1-16
[17] D.I. Svergun, Biophys J. 76 (1999) 2879-2886
[18] J. Pérez, A. Koutsioubas, Acta Cryst. D71 (2015) 86-93
[19] F. Spinozzi, F. Carsughi, P. Mariani, J. Chem. Phys. 109 (1998) 10148-10158
[20] J. Oberdisse, P. Hine, W. Pyckhout-Hintzen, Soft Matter 3 (2007) 476-485
[21] H. Endo, M. Mihailescu, M. Monkenbusch, J. Allgaier, G. Gompper, D. Richter, B. Jakobs, T. Sottmann, R. Strey, I. Grillo, J. Chem. Phys. 115 (2001) 580-600
[22] D.L. Ho, R.M. Briber, C.J. Glinka, Chem. Mater. 13 (2001) 1923-1931
[23] E. Loizou, P. Butler, L. Porcar, E. Kesselman, Y. Talmon, A. Dundigalla, G. Schmidt, Macromolecules 38 (2005) 2047-2049
[24] V. Causin, C. Marega, A. Marigo, G. Ferrara, Polymer 46 (2005) 9533-9537
[25] C. Marega, A. Marigo, G. Cingano, R. Zanetti Polymer 37 (1996) 5549-5557
[26] M.F. Brigatti, E. Galán, B.K.G. Theng, Structure and Mineralogy of Clay Minerals in F. Bergaya, B.K.G. Theng, G. Lagaly (Eds.), Handbook of Clay Science, Volume 5, Part A, Chapter 2, Elsevier - Oxford, 2013, pp. 21-81
[27] H.E. Hermes, H. Frielinghaus, W. Pyckhout-Hintzen, D. Richter, Polymer 47 (2006) 2147-2155
[28] J.S. Pedersen, Adv. Coll. Interf. Sci. 70 (1997) 171-210
[29] O. Glatter, O. Kratky, Small-angle X-ray Scattering, Academic Press, London (1982)

[30] J.S. Pedersen, P. Schurtenberger, Macromolecules 29 (1996) 7602-7612
[31] G. Beaucage, J. Appl. Cryst. 29 (1996) 134-146
[32] M. Siglreitmeier, B. Wu, T. Kollmann, M. Neubauer, G. Nagy, D. Schwahn, V. Pipich, D. Faivre, D. Zahn, A. Fery, H. Cölfen, Beilstein J. Nanotechnol. 6 (2015) 134–148
[33] Z. Tang, N.A. Kotov, S. Magonov, B. Ozturk, Nature Materials 2 (2003) 413-418
[34] X. Ye, T. Narayanan, P. Tong, J. S. Huang, M. Y. Lin, B. L. Carvalho, L. J. Fetters, Phys. Rev. E 54 (1996) 6500-6510
[35] G. Calas, W.A. Bassett, J. Petiau, M. Steinberg, D. Tchoubar, A. Zarka, Phys. Chem. Minerals 11 (1984) 17-36
[36] O. Kratky, G. Porod, J. Coll. Sci. 4 (1949) 35
[37] R.A. Vaia, W. Liu, J. Polym. Sci. Part B: Polym. Phys. 40 (2002) 1590-1600
[38] H.J.M. Hanley, C.D. Muzny, D.L. Ho, C.J. Glinka, Langmuir 19 (2003) 5575-5580
[39] T.D. Fornes, P.J. Yoon, H. Keskkula, D.R. Paul, Polymer 42 (2001) 9929-9940
[40] D.J. Chaiko, Chem. Mater. 15 (2003) 1105-1110
[41] A. Das, D.-Y. Wang, K.W. Stöckelhuber, R. Jurk, J. Fritzsche, M. Klüppel, G. Heinrich, Adv. Polym. Sci. 239 (2011) 85–166
[42] K. Nusser, S. Neueder, G.J. Schneider, M. Meyer, W. Pyckhout-Hintzen, L. Willner, A. Radulescu, D. Richter, Macromolecules 43 (2010) 9837–9847
[43] L.J. Fetters, D.J. Lohsey, R.H. Colby, Chain Dimensions and Entanglement Spacings, in J.E. Mark (Ed.), Physical Properties of Polymers Handbook, Chapter 25, Springer, New York 2007, pp. 447-454
[44] S. Gagliardi, V. Arrighi, R. Ferguson, A.C. Dagger, J.A. Semlyen, J.S. Higgins, J. Chem. Phys. 122 (2005) 064904
[45] D. Schwahn, K. Hahn, J. Streib, T. Springer, J. Chem. Phys. 93 (1990) 8383
[46] H. Frielinghaus, Flexible Polymers, in G. Gompper, U.B. Kaupp, J.K.G. Dhont, D. Richter, R.G. Winkler (Eds.), Physics meets Biology - From Soft Matter to Cell Biology, Schriften des Forschungszentrums Jülich, Jülich 2004, pp. C1.1-34
[47] L. Leibler, Macromolecules 13 (1980) 1602–1617
[48] H. Frielinghaus, N. Hermsdorf, R. Sigel, K. Almdal, K. Mortensen, I. W. Hamley, L. Messé, L. Corvazier , A. J. Ryan, D. van Dusschoten, M. Wilhelm, G. Floudas, G. Fytas, Macromolecules 34 (2001) 4907–4916 and P.D. Olmsted, I.W. Hamley, Europhys. Lett. 45 (1999) 83
[49] A. Botti, W. Pyckhout-Hintzen, D. Richter, V. Urban, E. Straube, J. Kohlbrecher, Polymer 44 (2003) 7505–7512
[50] A. Banc, A.-C. Genix, C. Dupas, M. Sztucki, R. Schweins, M.-S. Appavou, J. Oberdisse, Macromolecules 48 (2015) 6596-6605
[51] H. Frielinghaus, B. Abbas, D. Schwahn, L. Willner, Europhys. Lett. 44 (1998) 606-612
[52] D. Schwahn, K. Mortensen, H. Yee-Madeira, Phys. Rev. Lett. 58 (1987) 1544-1546
[53] V. Pipich, D. Schwahn, L. Willner, J. Chem. Phys. 123 (2005) 124904
[54] R.J. Hickey, T.M. Gillard, M.T. Irwin, T.P. Lodge, F.S. Bates, Soft Matter 12 (2016) 53-66
[55] A. Gambassi, A. Maciołek, C. Hertlein, U. Nellen, L. Helden, C. Bechinger, S. Dietrich, Phys. Rev. E 80 (2009) 061143
[56] S. P. Obukhov, A. N. Semenov, Phys. Rev. Lett. 95 (2005) 038305
[57] B. Duplantier, J. Stat. Phys. 54 (1989) 581-680
[58] H. Frielinghaus, X. Frielinghaus, N. Ruocco, J. Allgaier, W. Pyckhout-Hintzen, D. Richter, Soft Matter 9 (2013) 10484-10492
[59] L. Willner, A. Poppe, J. Allgaier, M. Monkenbusch, P. Lindner, D. Richter, Europhys. Lett. 51 (2000) 628-634

[60] J.S. Pedersen, D. Posselt, K. Mortensen, J. Appl. Cryst. 23 (1990) 321-333
[61] X. Frielinghaus, M. Brodeck, O. Holderer, H. Frielinghaus, Langmuir 26 (2010) 17444-17448
[62] B. Ewen, D. Richter, Adv. Polym. Sci. 134 (1999) 1-129
[63] A. Arbe, J. Colmenero, M. Monkenbusch, D. Richter, Phys. Rev. Lett. 83 (1998) 590-593
[64] S. Miyazaki, H. Endo, T. Karino, K. Haraguchi, M. Shibayama, Macromolecules 40 (2007) 4287-4295
[65] F. Lipfert, O. Holderer, H. Frielinghaus, M.-S. Appavou, C. Do, M. Ohl, D. Richter, Nanoscale 7 (2015) 2578-2586
[66] D.M. Anderson, H. Wennerström, J. Phys. Chem. 94 (1990) 8683-8694
[67] S. Maccarrone, H. Frielinghaus, J. Allgaier, D. Richter, P. Lindner, Langmuir 23 (2007) 9559-9562